J Solid State Electrochem (2016) 20:235–246
DOI 10.1007/s10008-015-3015-4

ORIGINAL PAPER

Peculiarities of structure, morphology, and electrochemistry of the doped 5-V spinel cathode materials $LiNi_{0.5-x}Mn_{1.5-y}M_{x+y}O_4$ (M=Co, Cr, Ti; $x+y=0.05$) prepared by mechanochemical way

N. V. Kosova[1] · I. A. Bobrikov[2] · O. A. Podgornova[1] · A. M. Balagurov[2] · A. K. Gutakovskii[3,4]

Received: 26 May 2015 / Revised: 20 July 2015 / Accepted: 11 August 2015 / Published online: 2 September 2015

Abstract The pure $LiNi_{0.5}Mn_{1.5}O_4$ and doped spinels $LiNi_{0.5-x}Mn_{1.5-y}M_{x+y}O_4$ (M=Co, Cr, Ti; $x+y=0.05$) were prepared by mechanochemically assisted solid state synthesis using a high-energy AGO-2 planetary mill. The activated samples were annealed at 700 and 800 °C in oxygen and then characterized by x-ray powder diffraction (XRD) and neutron powder diffraction (NPD) with Rietveld refinement, high-resolution transmission electron microscopy (HRTEM) and electron microdiffraction, Fourier transform infrared spectroscopy (FTIR), galvanostatic cycling and galvanostatic intermittent titration technique (GITT). The structure of the high-temperature (HT) samples (800 °C) is well refined with the single *Fd*-3*m* spinel. On the contrary, the low-temperature (LT) samples (700 °C) are two-phase spinels with the 5–10 % fraction of the $P4_332$ phase depending on the substitution ion. The dopants preferably substitute for Ni ions that correlates with the appearance of the $Li_yNi_{1-y}O$ by-product (3–7 %). The rock salt-structured phase was observed on the surface of the particles coherently conjugated with the LT spinel crystal bulk. For all doped samples, two pairs of redox peaks are observed on the dQ/dV plots revealing the prevalence of the disordered spinel phase. However, the separation between the peaks increases for the HT samples resulting in better charge-discharge performance as compared with the undoped spinel. Lithium diffusion coefficient (D_{Li+}) of the doped HT spinels estimated by GITT is two orders of magnitude higher than that of the undoped spinel. The highest rate capability is observed for the Ti-doped HT spinel due to larger lattice parameter.

Keywords Doped $LiNi_{0.5}Mn_{1.5}O_4$ · Mechanical activation · NPD · HRTEM · Electrochemical cycling · GITT

✉ N. V. Kosova
kosova@solid.nsc.ru

[1] Institute of Solid State Chemistry and Mechanochemistry SB RAS, 18 Kutateladze, Novosibirsk, Russia 630128

[2] Joint Institute for Nuclear Research, 6 Joliot-Curie, Dubna, Russia 141980

[3] Rzhanov Institute of Semiconductor Physics SB RAS, 13 pr. Acad. Lavrent'ev, Novosibirsk, Russia 630090

[4] Novosibirsk State University, 2 Pirogova, Novosibirsk, Russia 630090

Introduction

The lithium nickel manganese spinel $LiNi_{0.5}Mn_{1.5}O_4$ is the most promising among the 5-V cathode materials for lithium-ion batteries due to a flat plateau at 4.7 V and a two-electron process $Ni^{2+/4+}$, while the Mn^{4+} ions remain electrochemically inactive [1, 2]. Two crystal structures of $LiNi_{0.5}Mn_{1.5}O_4$ can be formed depending on the synthesis conditions. A primitive cubic spinel with a space group $P4_332$ and 3*d* cation ordering is formed at $T\leq700$ °C, while a face-centered spinel with a space group *Fd*-3*m* and statistical distribution of 3*d* cations is formed at $T\geq800$ °C [3]. Thermally induced order→disorder transition occurs between 700 and 730 °C [4] and is driven by the oxygen deficiency, resulting in the appearance of the Mn^{3+} ions to satisfy the charge balance in the spinel structure. The formation of the high-temperature polymorph is always accompanied by the appearance of the rock salt impurity phase. Recently, an alternative to this two-phase model, namely the partial ordering of Ni and Mn within the $P4_332$ phase, has been proposed by Cabana et al. [5]. Shin et al. [6] suggested that the "disordered" samples consist of a minority fraction with a cation disorder on the transition metal site and a majority fraction

of small-ordered domains that are disordered with respect to each other within larger particles.

In the $P4_332$-structured $LiNi_{0.5}Mn_{1.5}O_4$, the Li atoms are located at the 8*c* sites, the Ni atoms at the 4*c* sites, the Mn atoms at the 12*d* sites, and the O atoms at the 8*c* and 24*e* sites. Within the *Fd*-3*m* structure, the Ni and Mn atoms are randomly distributed in the 16*d* sites, while the Li and O atoms occupy the 8*a* and 32*e* sites, respectively. The ordered and disordered modifications of $LiNi_{0.5}Mn_{1.5}O_4$ differ in their electrochemical behavior and phase transitions observed during Li insertion and extraction. Despite a flat voltage profile, slightly larger initial capacity and higher cell voltage, the ordered spinel $LiNi_{0.5}Mn_{1.5}O_4$ ($P4_332$) shows poorer electrochemical behavior than the disordered one (*Fd*-3*m*), which is mainly due to the structural transformations during cycling. While the disordered spinel undergoes one topotactic two-phase transition, the ordered one shows the topotactic phase transitions among three different cubic phases [7]. The inferior rate capability of the ordered spinel has been explained by (i) the strain associated with the additional phase transition and (ii) lower ionic and electronic conductivity [4, 8].

To minimize the influence of the structural transformations on capacity retention and to increase the particles' adaptability to the volume changes, cation substitution and nanosizing can be used. Cation doping is considered to be an effective way to modify the intrinsic properties of the electrode materials. Many various elements have been proposed by different research groups to impact the $LiNi_{0.5}Mn_{1.5}O_4$ structure, electrical conductivity, its stability on Li insertion/deinsertion, and capacity retention on cycling, including Co [9–11], Cr [12, 13], Ti [14–16], etc. It has been established that the metal dopants improved the electrochemical performance by promoting a statistical distribution of Ni and Mn ions in the 16*d* sites, eliminating the $Li_yNi_{1-y}O$ impurity, improving electronic conductivity (due to Mn^{3+} introduction) and Li^+ diffusion (due to an increase in the lattice parameter), and decreasing the undesired solid electrolyte interface (SEI) films by enriching with the dopants and generating the Ni ions deficiency on the surface [1].

On the other hand, the creation of nanostructures is a popular strategy to increase rate capability due to a drastic reduction of Li^+ diffusion lengths, larger electrode-electrolyte contact area leading to higher charge-discharge rates, while the disadvantages of nanostructured materials include an increase in undesirable electrode-electrolyte reactions due to a high surface area, leading to self-discharge, poor cycling, and calendar life. Xue et al. [17] concluded that the suitable particle size was required to achieve the best performance of $LiNi_{0.5}Mn_{1.5}O_4$ in terms of rate capability and cyclic stability. The as-received results have demonstrated that $LiNi_{0.5}Mn_{1.5}O_4$ with its particle size, limited between micro and nano, exhibited the best electrochemical properties. According to Yang et al. [18], a micron-sized disordered phase and a nano-sized ordered phase of $LiNi_{0.5}Mn_{1.5}O_4$ display the best combination for high-rate capability and cycling performance.

The crystal structure, morphology, surface composition and, as a result, the electrochemical properties of $LiNi_{0.5}Mn_{1.5}O_4$ strongly depend on the synthesis method. Ni/Mn ordering and the amount of the rock salt impurity are the main controllable factors in the synthesis, that determine the electrochemical properties. However, the question on the influence of different degree of Ni/Mn cation ordering on the electrochemical performance of $LiNi_{0.5}Mn_{1.5}O_4$ is still controversial. The conventional solid state method has been reported to be unsuccessful for the synthesis of high-performance $LiNi_{0.5}Mn_{1.5}O_4$ so far due to formation of Ni oxide impurities and the local inhomogeneity of the micron-sized material owing to the large diffusion paths between the particles during the synthesis process. Although the various solution techniques including the sol-gel, co-precipitation, and hydrothermal methods provide the high quality $LiNi_{0.5}Mn_{1.5}O_4$ powder [1], these preparation methods are multi-step processes of high cost. Therefore, the development of a simple synthesis route for the preparation of the $LiNi_{0.5}Mn_{1.5}O_4$ powder is important. Mechanical activation (MA) or high-energy ball-milling is a simple energy- and eco-efficient advanced method to prepare highly homogeneous mixtures of powders of several species in contrast to the traditional solid state synthesis [19–24]. It is believed that the high homogeneity of the multicomponent reagent mixture prepared by MA helps to synthesize phase-pure $LiNi_{0.5}Mn_{1.5}O_4$. Kozawa et al. [24] reported a rapid synthesis of the $LiNi_{0.5}Mn_{1.5}O_4$ spinel by mechanochemical process using an attrition-type mill with a rotation speed of a rotor of 4500 rpm. The as-obtained micrometer particles of the product composed of the aggregated nano-sized particles allowed the authors to achieve both excellent rate capability and high volumetric energy density. Besides, a granular structure and a bimodal distribution of the as-prepared powder led to a high packing density of the electrode.

The goal of the present work was a comparative study of the substitution effect on the structure, morphology, and electrochemistry of $LiNi_{0.5-x}Mn_{1.5-y}M_{x+y}O_4$ (M=Co, Cr, Ti; $x+y=0.05$) prepared by mechanochemically assisted solid state synthesis using a combination of different physico-chemical methods. The chosen dopants have different charge (Co^{3+}, Cr^{3+}, Ti^{4+}), ionic radius (R_{Co3+}=0.545 Å, R_{Cr3+}=0.615 Å, R_{Ti4+}=0.605 Å) [25] and electronic configuration in the final products (Co $3t_{2g}^6$, Cr $3t_{2g}^3$, Ti $3t_{2g}^0$).

Experimental

The pure $LiNi_{0.5}Mn_{1.5}O_4$ and doped $LiNi_{0.5-x}Mn_{1.5-y}M_{x+y}O_4$ (M=Co, Cr, Ti; $x+y=0.05$) spinels were prepared by mechanochemically assisted solid state synthesis using

stoichiometric amounts of lithium carbonate (Li_2CO_3), manganese oxide (MnO), nickel oxide (NiO), cobalt hydroxide ($Co(OH)_2$), chromium acetate ($Cr(CH_3COO)_3$), and titanium oxide (TiO_2) (anatase) (qualification "pure for analysis"). Mechanical activation (MA) of the reagent mixtures was performed using a high-energy AGO-2 planetary mill (Novic, Novosibirsk, Russia) in Ar atmosphere for 5 min (1000 rpm, powder to balls mass ratio 1:40). The activated mixtures were subsequently annealed at 700 and 800 °C in oxygen atmosphere for 6 h and naturally cooled in a furnace. The composition of the reagent mixtures was based on electroneutrality by considering the charge of the doping ions in the final products after annealing the activated mixtures in oxygen: $LiNi_{0.475}Mn_{1.475}Co_{0.05}O_4$, $LiNi_{0.475}Mn_{1.475}Cr_{0.05}O_4$, and $LiNi_{0.5}Mn_{1.45}Ti_{0.05}O_4$. The low-temperature (700 °C) and high-temperature (800 °C) annealed samples are further labeled as the LT and HT samples, respectively.

X-ray powder diffraction (XRD) was performed using a Bruker D8 Advance diffractometer, Cu $K\alpha$ irradiation (λ= 1.5418 Å). The XRD patterns were collected over the range of 15–85 ° with a step of 0.02 ° s^{-1} and uptake time of 0.3–0.5 s. The neutron powder diffraction (NPD) experiments were carried out using a reverse time-of-flight (RTOF) high-resolution diffractometer (HRFD) at the IBR-2 pulsed reactor (JINR, Dubna) [26]. The resolution $\Delta d/d$ (where d is an interplanar distance) of this diffractometer is ~0.001 and it is nearly independent of d_{hkl}. The structural refinement of the XRD and NPD data was performed by Rietveld method using the FullProf software package. The high-resolution transmission electron microscopy (HRTEM) studies were performed using a JEM-4000EX microscope operated at 4000 kV with a point to point resolution of 0.16 nm. The Fourier transform infrared (FTIR) spectra were recorded using a BOMEM FTIR spectrometer (pellets with CsI).

For electrochemical testing, the composite cathodes were fabricated by mixing 80 wt% active material with 15 wt% Super P conductive carbon (Timcal Ltd.) and 5 wt% PVDF/NMP binder. The mixed slurry was then pasted on the aluminum foil to obtain the working electrodes. A loading density of the prepared samples was 2–3 mg cm^{-2}, and an electrode diameter of 10 mm was used throughout. The working electrodes were dried at 120 °C before cell assembly. The Swagelok-type cells were assembled in an argon-filled glovebox with Li as an anode; 1 M $LiPF_6$ (Sigma Aldrich, 99.99 %) solution in a mixture of ethylene carbonate (EC) and dimethylcarbonate (DMC) (Alfa Aesar, 99 %) 1:1 by weight as an electrolyte; and a glass fiber filter (Whatman, Grade GF/C) as a separator. Cycling was performed using a galvanostatic mode at the C/10-5C charge-discharge rates in the range of 3.0–4.85 V vs. Li/Li^+ at room temperature. The galvanostatic intermittent titration technique (GITT) measurements were carried out at the C/10 rate (I_0=14.7 mA g^{-1}) by applying a galvanostatic step of 10 min and a relaxation time of 1 h.

Results and discussion

XRD and NPD study

Figure 1 shows the XRD patterns of the pure $LiNi_{0.5}Mn_{1.5}O_4$ and doped $LiNi_{0.5-x}Mn_{1.5-y}M_{x+y}O_4$ (M=Co, Cr, Ti; $x+y$= 0.05) spinels prepared at 700 and 800 °C and Fig. 2 displays the Rietveld refined XRD patterns of the sample with the "$LiNi_{0.475}Mn_{1.475}Cr_{0.05}O_4$" nominal composition prepared at both temperatures as a representative example. It was found that the main reflections for all samples belonged to the spinel, while the low-intensive reflections belonged to the $Li_yNi_{1-y}O$ impurity. The reflections of the main phase become more intensive and narrow for the samples prepared at 800 °C due to higher crystallinity and larger crystallite size. It is reported that the relative peak intensities reflect the dominant surface orientations of the particles. The intensities of the (111), (400), and (440) reflections for all LT and HT samples were normalized by the (311) peak. The results are presented in Fig. 3. It is seen that the samples have nearly the same relative intensity ratio for all the indicated peaks. This observation suggests that the more high-active facets (111), (100), and (110) as formed will be beneficial for achieving good cycleability.

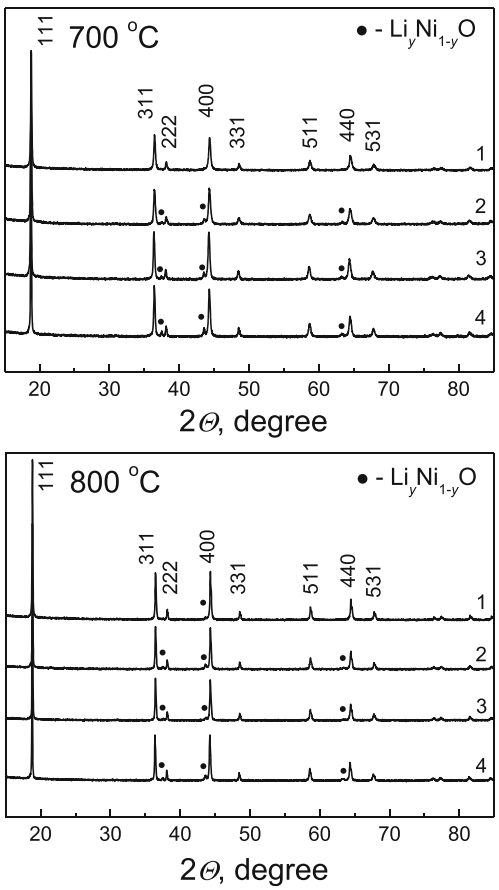

Fig. 1 XRD patterns of $LiMn_{1.5}Ni_{0.5}O_4$ (*1*) and the Co- (*2*), Cr- (*3*), and Ti- (*4*) doped spinels prepared at 700 and 800 °C

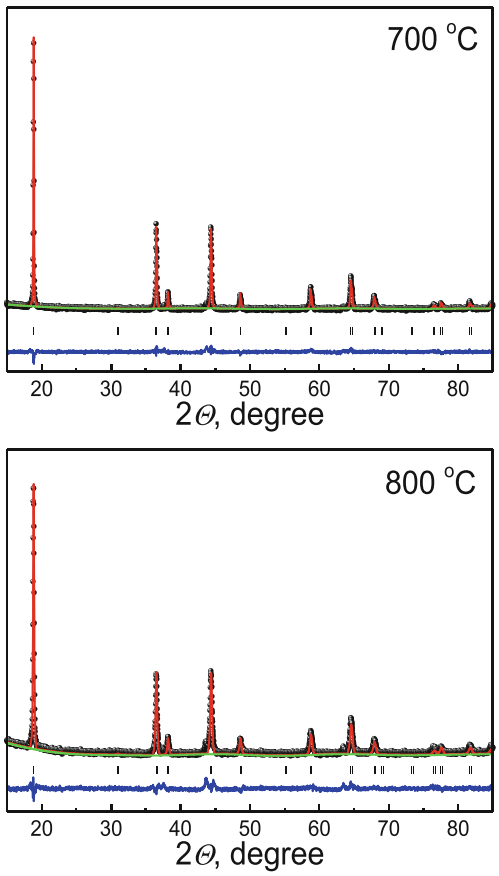

Fig. 2 Rietveld refined XRD patterns of the Cr-doped spinel prepared at 700 and 800 °C

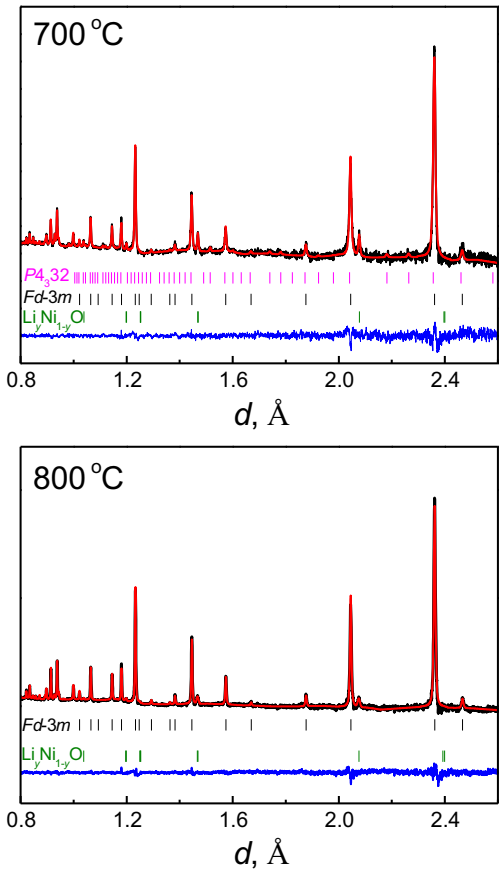

Fig. 4 Rietveld refined NPD patterns of the Cr-doped spinel prepared at 700 and 800 °C

Unfortunately, XRD is not a suitable tool for characterization of Ni/Mn distribution because Ni and Mn have nearly the same x-ray scattering power. Alternatively, NPD has a strong ability to differentiate the Mn and Ni ions due to the huge difference in the coherent scattering lengths (b_{Ni}=10.3 fm, b_{Mn}=−3.73 fm), which makes it an advantageous tool to probe Ni/Mn cation ordering. The most appropriate way to refine the structure and composition is to use the combined XRD and NPD data. Figure 4 shows the refined NPD patterns of the LT and HT Cr-doped spinels as an example.

According to the Rietveld refinement of the NPD data, the structure of the undoped and doped HT samples is well refined with a one-phase model as a *Fd*-3*m* spinel. On the contrary, the patterns of the undoped and doped LT samples can be well refined with a two-phase model as a combination of a *Fd*-3*m* spinel as a dominant phase and a $P4_332$ phase as a secondary one with a fraction of 5–10 % depending on the substitution ion (see Table 1). Based on the NPD data, we cannot exclude the existence of the short-ordering domains in the LT samples. Note that almost full *Fd*-3*m*→$P4_332$ transformation is reported to occur after additional annealing the *Fd*-3*m* phase at 700 °C. However, in this work, the doped LT samples consist of predominantly *Fd*-3*m* phase and the small amounts of the rock salt-structured impurity $Li_yNi_{1-y}O$ are present in both LT and HT samples, probably due to the rapid one-step synthesis. The refined fraction of the $Li_yNi_{1-y}O$ phase is about 5–7 % for the LT samples and 2–6 % for the HT samples. The appearance of the $Li_yNi_{1-y}O$ by-product is a result of the preferable

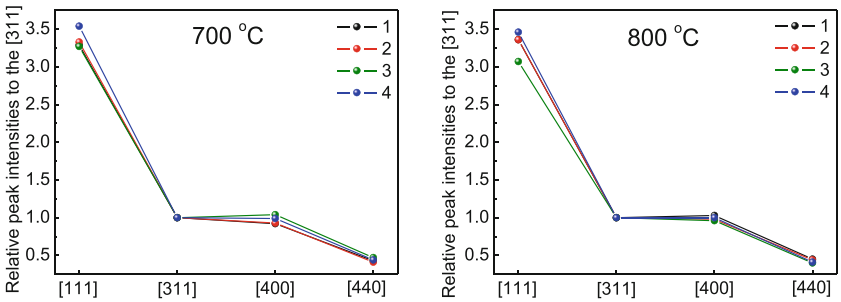

Fig. 3 Relative XRD peak intensities of the spinels prepared at 700 and 800 °C normalized by the (311) peak. *1* undoped $LiMn_{1.5}Ni_{0.5}O_4$, *2* Co, *3* Cr, and *4* Ti-doped spinels

Table 1 Refined lattice parameters of the undoped $LiMn_{1.5}Ni_{0.5}O_4$ and doped $LiNi_{0.5-x}Mn_{1.5-y}M_{x+y}O_4$ (M=Co, Cr, Ti; $x+y=0.05$) spinels from NPD data

Lattice parameter	Undoped spinel		Co (R_{Co3+}=0.545 Å)		Cr (R_{Cr3+}=0.615 Å)		Ti (R_{Ti4+}=0.605 Å)	
	700 °C	800 °C	700 °C	800 °C	700 °C	800 °C	700 °C	800 °C
a, Å	8.1697 (3)	8.1710 (1)	8.1739 (3)	8.1762 (1)	8.1754 (3)	8.1784 (1)	8.1819 (3)	8.1849 (1)
V, Å^3	545.28 (5)	545.54 (2)	546.13 (3)	546.58 (2)	546.42 (3)	547.03 (2)	547.74 (3)	548.34 (2)
Fd-3*m*/*P*4$_3$32/$Li_yNi_{1-y}O$ ratio, %	–/100/–	95.9/–/4.1	87.2/5.2/7.6	93.2/–/6.8	85.1/9.4/5.5	97.2/–/2.8	84.5/10.4/5.1	96.5/–/3.5
χ^2	1.83	1.27	1.93	2.44	1.40	2.08	2.43	1.89
R_{wp}, %	4.10	3.88	4.28	3.89	3.80	3.71	4.13	3.66

substitution of the dopants for Ni ions. Earlier, it has been established that the phase composition of this by-product might vary depending on the calcination temperature leading to the appearance of NiO, $Li_yNi_{1-y}O$, $(Li_xMn_{0.66}Ni_{0.34})_yO$ [5], or $(Li_{0.33}Mn_{0.5}Ni_{0.167})_yO$ [27]. The formation of the rock salt phase requires a transfer of Ni and/or Mn to the interstitial octahedral sites (16*c*), thus displacing the Li^+ ions from the tetrahedral sites (8*a*) to the octahedral sites (16*c*), while the oxygen ions retain a face-centered cubic array [28]. Therefore, the rock salt phase can be only generated above 700 °C when the Ni and/or Mn ions become mobile. Meanwhile, it has been noted that at high temperatures, the transition of the spinel to the rock salt phase was reversible. Unfortunately, due to the very low concentration of the rock salt-structured impurity phase in the samples and partial overlapping of its reflections with the strong reflections from the spinel, it was rather difficult to evaluate its precise composition.

The refined lattice parameters of the samples studied are presented in Table 1. It is seen that the lattice parameters for the doped spinels are very close to each other and slightly increase with annealing temperature, which correlates with the increased concentration of the Mn^{3+} ions (R_{Mn3+}= 0.58 Å) instead of the Mn^{4+} ions (R_{Mn4+}=0.53 Å) in the samples, estimated from the galvanostatic cycling data, but not with the changes in the ionic radius of the dopants since the amount of a dopant is much lower than the concentration of the Mn^{3+} ions. Unlike $LiMn_2O_4$, the Jahn-Teller effect caused by the presence of Mn^{3+} is not an issue for $LiNi_{0.5}Mn_{1.5}O_4$ as long as the discharge cutoff voltage is above 3 V vs. Li/Li^+. Although we tried to refine the oxygen occupancies in the spinel phases, we could not find a reasonable amount of the oxygen vacancies using either a two-phase or a one-phase model. It is assumed that relatively small oxygen vacancy contents in the spinel may make it less sensitive and challenging for the refinements. The charge balance in the absence of oxygen vacancies is achieved by the replacement of the Mn^{4+} ions by the Mn^{3+} ions. Manganese excess coupled with Ni deficiency (due to a partial transition of the Ni^{2+} ions to the rock salt-structured impurity) was found for all as-prepared samples. Comparing the values of Gibbs energy for NiO, MnO_2, Co_3O_4, Cr_2O_3, and TiO_2 at 298 K, which are equal to −239.7, −521.0, −915.0, −1140.6, and −944.0 kJ mol^{-1}, respectively [29], one can imagine that larger bonding energy between the transition metal dopant and oxygen can change the resulting covalency and intensify bonding strength of transition metal ion with oxygen in the doped spinels, leading to their structural and chemical stability.

FTIR study

The cation ordering in $LiNi_{0.5}Mn_{1.5}O_4$ can be additionally characterized by FTIR spectroscopy. A comparison of the 588 cm^{-1} Ni–O band and the 620 cm^{-1} Mn–O band in the FTIR spectra is considered to be a semi-quantitative measure of the cation ordering fraction in the spinel samples [4]. The appearance of the well-defined bands at 430, 467, and 555 cm^{-1} is a signature of the ordered *P*4$_3$32 phase as a result of reduction of the space symmetry from the disordered to the ordered phase. Figure 5 shows that the intensity ratio of these lines in the spectra of the undoped LT spinel $LiNi_{0.5}Mn_{1.5}O_4$ is noticeably lower than that of the HT spinel, thus indicating higher degree of Ni/Mn ordering. On the other hand, the FTIR spectra of the doped spinels prepared at both synthesis temperatures suggest a high degree of cation disordering, as follows from the absence of the indicated bands and the low intensity ratio of the 588 cm^{-1} peak to the 620 cm^{-1} peak. These data are in agreement with the results of the NPD analysis.

According to Ref. [6], the intensity ratios of the FTIR bands may reflect the domain size of cation ordering and the presence of antiphase boundaries between domains (disorder between domains) rather than simply the degree of cation disorder on the transition metal site. However, the FTIR data are unable to indicate clearly the simultaneous presence of the short- and long-range cation orders in the samples.

TEM and HRTEM

According to the transmission electron microscopy (TEM) study, the average crystal size of the undoped LT and HT

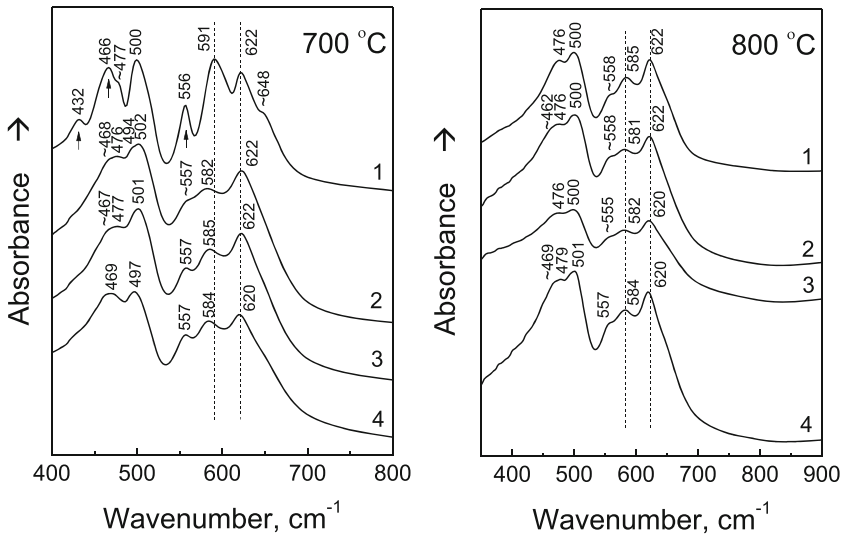

Fig. 5 FTIR spectra of $LiMn_{1.5}Ni_{0.5}O_4$ (*1*) and the Co- (*2*), Cr- (*3*), and Ti- (*4*) doped spinels prepared at 700 and 800 °C

spinels is 50–100 and 100–150 nm, respectively, while doping facilitates the crystal growth, resulting in larger particles with narrow size distribution. Figure 6 shows the TEM images of the typical Cr-doped crystals prepared at 700 and 800 °C. According to the statistical analysis of the similar images, the average crystal size is 100–300 nm for the LT sample and 200–400 nm for the HT sample. The nanoparticles have an evident faceting. The crystallographic directions of faceting coincide with the intersections of the {111} planes and the surface of the crystal, oriented normally to the electron beam direction (shown in round brackets). Lee and Persson [30] have determined that the {111} facet has the lowest surface

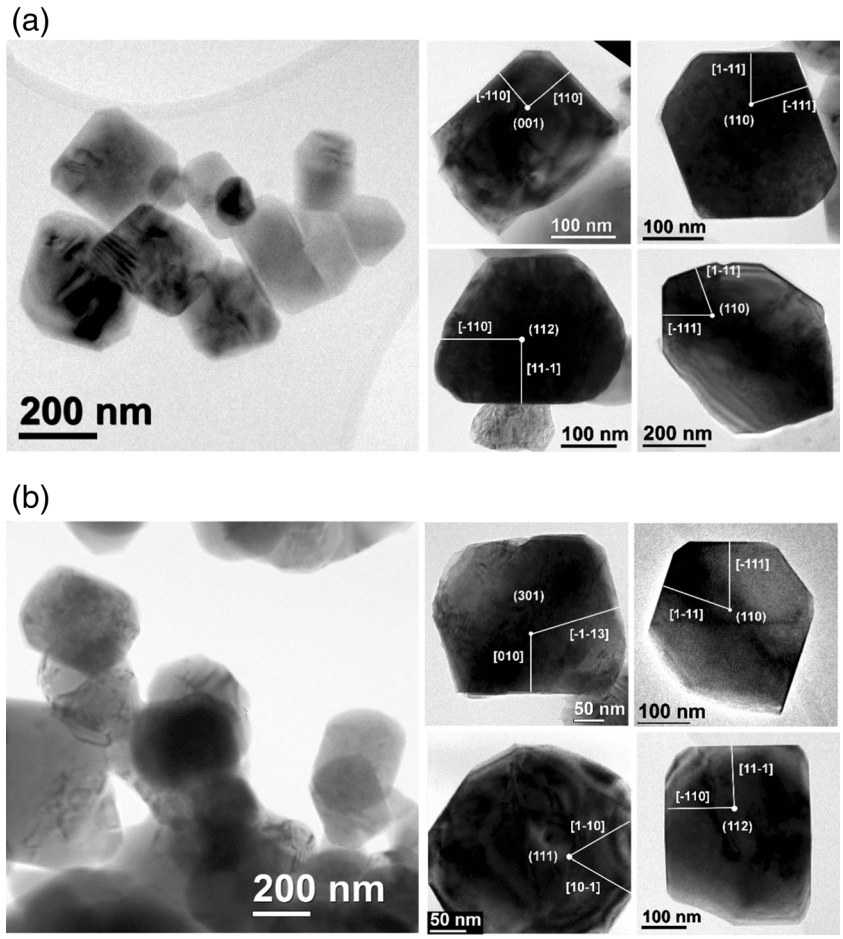

Fig. 6 TEM images of the typical crystals of the Cr-doped spinels prepared at 700 °C (**a**) and 800 °C (**b**)

energy, followed by the {100} and {110} facets, and therefore, dominates in the growth process, resulting in an equilibrium cubo-octahedral particle morphology and exhibiting the best stability upon cycling.

The analysis of the HRTEM images and the selected area electron diffraction (SAED) patterns indicates that in both Cr-doped samples, there are the crystals of the *Fd*-3*m* spinel with the lattice parameter equal to 0.8170 nm (Fig. 7). In addition to the crystals with the disordered spinel structure in the LT sample, one can clearly see the HRTEM images of the crystals with the atomic planes located between the {111} facets, i.e., the {222} facets (Fig. 7B-b). The interplanar distance {111} in these crystals is the same (0.47 nm). On the SAED patterns, the intensity of their even order reflections increases (Fig. 7B-c). The appearance of the reflections from the (002) planes in the spinels with the *Fd*-3*m* space group can be a result of two factors. The first and the main one is associated with the 100–300-nm thickness of the crystals analyzed by SAED. For such a thickness, the dynamic conditions of diffraction, but not the kinematic ones, are realized. For dynamic diffraction, the reflections from the (002) planes are permitted. Secondly, the reflections from the (002) planes may have appeared because of the difference in the atomic factors of electron scattering on the different atoms even at kinematic diffraction. Thus, the SAED patterns indicate the formation of the second phase with the $P4_332$ space group in the LT sample.

An interesting peculiarity of the structure of some crystals of the doped LT samples, prepared by mechanochemically assisted method, has been established. Along the perimeter of these crystals, we have observed the presence of another phase, coherently conjugated with the crystal bulk. Figure 8b shows the fragment of the phase corresponding to the part of the crystal, marked by the white square in Fig. 8a. The enlarged HRTEM images of the areas 1 (2) and 3 are depicted in Fig. 8c, d, while Fig. 8e, f show the corresponding SAED patterns. It is evident that the structure of the crystal fragment in area 3 is similar to the structure of the crystal in Fig. 7a. In the areas 1 and 2, the interplanar distances {111} increase up to ~0.52 nm. The SAED pattern in Fig. 8e corresponds to area 2 and partially to area 3 and contains the reflections from both the crystal bulk (reflections {111} marked with "b") and the surface phase (reflections {111} marked with "s"). The latter is probably an impurity phase with a *Fm*-3*m* space group that appears to grow on the corner of the octahedral particle of the spinel due to reconstruction to the Ni-rich (relative to the overall Ni/Mn ratio) rock salt-structured phase. This involves the migration of nickel ions toward the surface, thus resulting in the formation of a "core-shell" composite, where the spinel is a "core" and the rock salt-structured impurity is a "shell." The HT sample retained the disordered spinel structure over all parts of the material, both in the surface and bulk inside.

Galvanostatic cycling

According to the literature data [8], the degree of ordering (or the size of the ordered domains) is responsible for the electrochemical performance of $LiNi_{0.5}Mn_{1.5}O_4$. Higher degree of ordering increases open-circuit voltage (OCV) and initial capacity, but reduces the cycle life and rate capability. Amatucci et al. [4] have found that the disordered phase had Li diffusion coefficient two orders of magnitude higher than the ordered

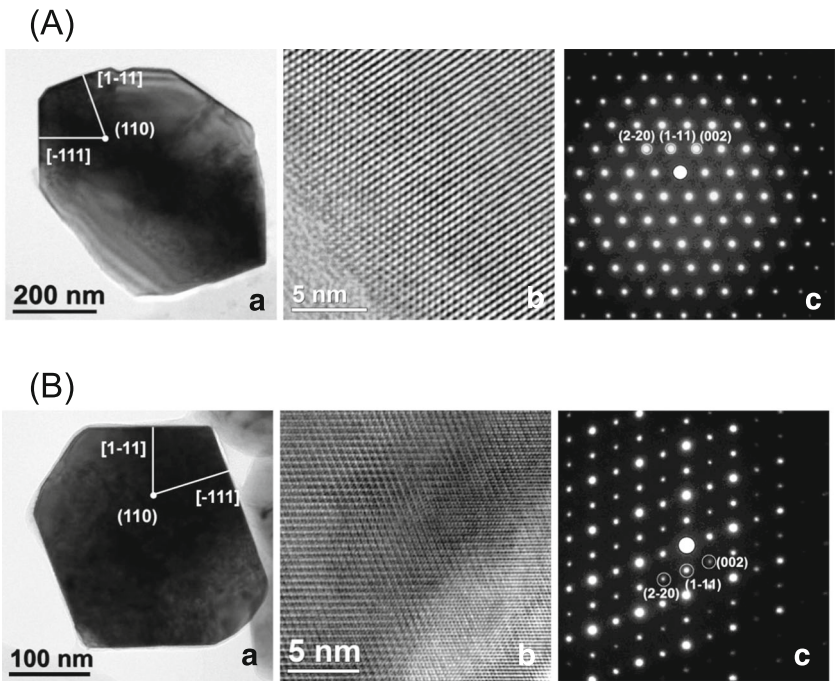

Fig. 7 TEM (a) and HRTEM (b) images and SAED patterns (c) of two typical crystals of the Cr-doped spinel prepared at 700 °C. **A** Single-phase spinel (*Fd*-3*m*); **B** Double-phase spinel (*Fd*-3*m* and $P4_332$)

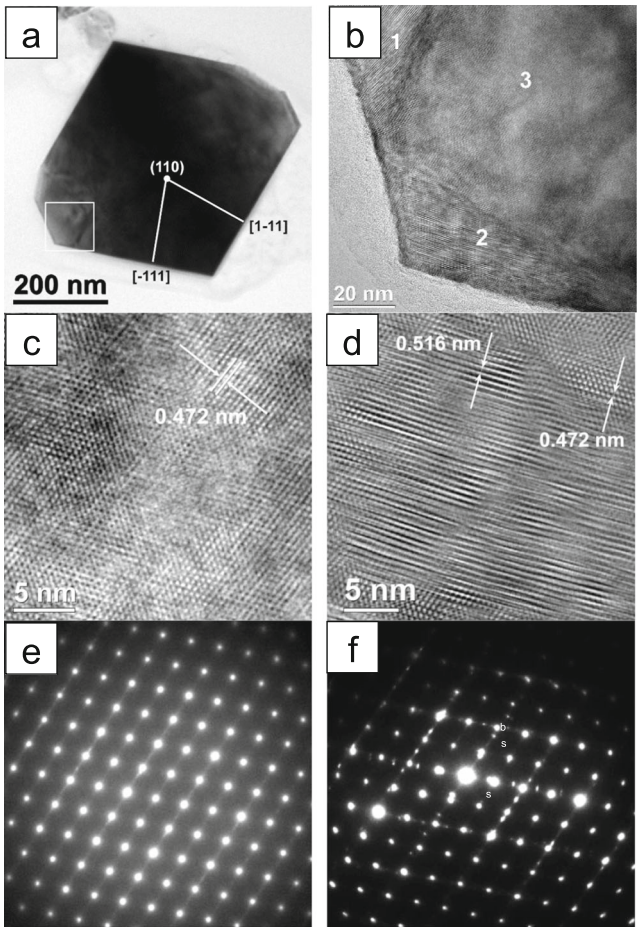

Fig. 8 TEM (**a**) and HRTEM (**b**) images of the Cr-doped spinel prepared at 700 °C. Enlarged HRTEM images (**c**, **d**) and SAED patterns (**e**, **f**) corresponding to the areas 3 (**c**, **e**) and 1, 2 (**d**, **f**), respectively

counterpart. The presence of the Mn^{3+} ions in the disordered spinel contributes to the conductivity enhancement, leading to the cycle life improvement, while the ordered phase is limited by its low electronic conductivity (10^{-7} S cm^{-1}).

The variation in cation ordering makes the charge-discharge profiles different, as seen in Fig. 9. It is related to the differences in the lithium-ion insertion energies between the ordered and disordered spinels. The ordered spinel has almost a single plateau in the 4.7 V region (the Ni^{2+}/Ni^{4+} redox couple), whereas the disordered spinel exhibits a distinct two-step plateau and an additional small plateau of the varying lengths in the 4.0 V region (the Mn^{3+}/Mn^{4+} redox couple). The length of the plateau in the 4.0 V region is a diagnostic of the changes in the Mn^{3+} content. Note that the Co and Cr dopants are present in the spinel in the 3+ oxidation state, while Ti is in the 4+ oxidation state. Therefore, even a small substitution of Co^{3+}, Cr^{3+}, and Ti^{4+} for Ni^{2+} in $LiNi_{0.5-x}Mn_{1.5-y}M_{x+y}O_4$ lowers the average manganese valence below 4+ with generation of the Mn^{3+} ions. The formation of the $Li_yNi_{1-y}O$ impurity is another reason to produce the Mn^{3+} ions.

Figure 9a shows that among all as-prepared spinels only undoped LT-$LiNi_{0.5}Mn_{1.5}O_4$ displays a flat plateau at 4.7 V during the charge-discharge processes, characteristic of the ordered phase. The plateau at 4 V is practically absent indicating the lack of the Mn^{3+} ions in its structure. The HT-$LiNi_{0.5}Mn_{1.5}O_4$ spinel and all doped spinels show two distinct plateaus at around 4.7 V and an additional plateau at 4 V. For the doped spinels prepared at 800 °C, the length of the 4 V plateau increases. An increase in the area of the ~4 V peak with increasing annealing temperature is shown in Fig. 10 and is attributed to a decrease in the average oxidation state of the Mn ions in the as-prepared spinels. For the undoped spinel, the amount of the Mn^{3+} ions, determined from the initial charge curves, increases with the synthesis temperature from ~0 (700 °C) to 0.2 Mn^{3+} (800 °C) per formula unit (f.u.); for the Co-, Cr-, and Ti-doped spinels, it increases from 0.14, 0.12, and 0.12 per f.u. (700 °C) to 0.19, 0.14, and 0.17 per f.u. (800 °C), respectively. Thus, the minimal changes in the concentration of the Mn^{3+} ions vs. the synthesis temperature were observed for the Cr-doped samples. These amounts of the Mn^{3+} ions correlate well with the total charge changes calculated from the aliovalent dopant substitution of the Ni^{2+} ions and from the $Li_yNi_{1-y}O$ amount, refined from the NPD data.

A more detailed analysis of the electrochemical behavior is further possible with the dQ/dV vs. voltage plots. Two pairs of the redox peaks are present on the dQ/dV plots in the 4.3–4.85 V range (Fig. 9b). It is seen that the separation between two oxidation and two reduction peaks increases for the HT samples due to an increase in cation disordering. For the LT samples, where the amount of the ordered phase is increased, the lower voltage peak is shifted to the higher voltage region close to the higher voltage peak. It is related to the charge-discharge mechanism of the spinel. The mechanism of Li insertion/extraction into/from the ordered spinel $Li_xNi_{0.5}Mn_{1.5}O_4$ (S.g. $P4_332$) was first studied by Ariyoshi et al. [31]. In the range from $x=1$ to $x=0$, two cubic/cubic two-phase reactions occur (at 4.72 and 4.74 V vs. Li/Li^+), with the intermediate definite composition at $x=0.5$ exhibiting a *Fd*-3*m* symmetry: $a=8.17/a=8.09$ at the Ni^{2+}/Ni^{3+} transition and $a=8.09/a=8.00$ at the Ni^{3+}/Ni^{4+} transition upon charging, accompanied by a 6 % change in the lattice volume. The authors supposed that the phase II was necessary as a buffer to accommodate the cell mismatch between the two end phases during lithium deinsertion. Kim et al. [7] observed the distinct mechanisms of the structural changes for the ordered and disordered spinels. While the ordered spinel shows the topotactic phase transition among three different cubic phases upon Li extraction (cations disordering operates during charge), the disordered spinel exhibits one-phase process from $x=1$ to $x\sim0.25$ followed by a two-phase process from $x\sim0.25$ to $x=0$ (both phases have a cubic symmetry). However, Lee and Persson [32] speculated that the small voltage step in the

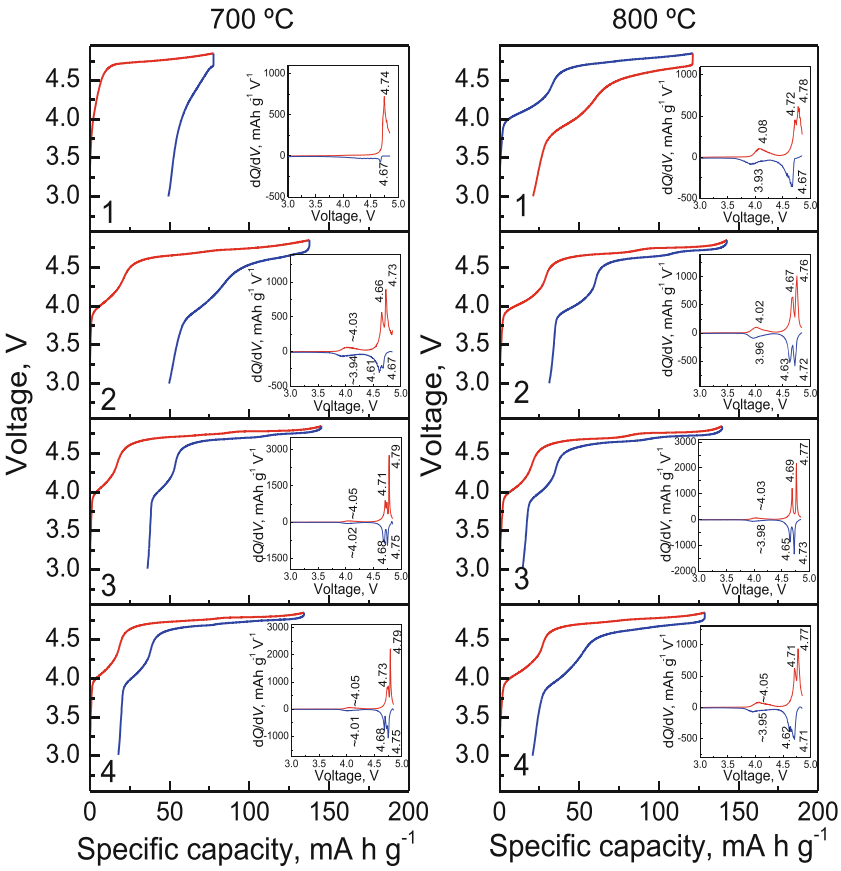

Fig. 9 Charge-discharge profiles and dQ/dV vs. voltage plots (in *insets*) in the 3.0–4.85 V range for $LiMn_{1.5}Ni_{0.5}O_4$ (*1*) and the Co- (*2*), Cr- (*3*), and Ti- (*4*) doped spinels prepared at 700 and 800 °C

$P4_332$ spinel might be due to a small partial cation disorder in the measured samples.

According to Fig. 11, the doped HT spinels show high capacity (~120 mA h g^{-1}) and good cycleability in the 3.0–4.85 V range, most probably due to higher content of the Mn^{3+} ions and lower content of the rock salt-structured impurity identified by XRD and NPD and practically full absence of the ordered $P4_332$ phase (or the sizes of the ordered domains) estimated by peak separation on the dQ/dV vs. voltage plots. The capacity should be increased by extension of the high cutoff to 5 V and using more stable electrolytes. Meanwhile, the Ti-doped HT spinel displays the best high-rate capability, probably due to larger lattice parameter of the spinel determining the cross section of the channels for Li diffusion (Fig. 12). It has been noticed that larger lattice constant region in disordered $LiNi_{0.5}Mn_{1.5}O_4$ was associated with an increase in the Mn^{3+}/Mn^{4+} ratio and a strong continuous increase in conductivity that had occurred until the critical point at 0.81765 nm was reached [4]. Amatucci et al. [4] showed that after this point, conductivity becomes independent of the lattice constant. Except the size effect on the cycleability, the authors [15] consider that the Ti substitution suppresses the phase transformation of $LiNi_{0.5}Mn_{1.5}O_4$ during delithiation.

The LT samples showed a noticeable deterioration upon cycling. There are four main problems resulting in the capacity fade for the $LiNi_{0.5}Mn_{1.5}O_4$ materials: (1) formation of a solid electrolyte interface (SEI) layer through the undesired side reactions with the electrolyte, (2) cationic ordering between the Mn^{4+} ions and the Ni^{2+} ions decreasing the electronic conductivity, (3) formation of the $Li_yNi_{1-y}O$ impurity

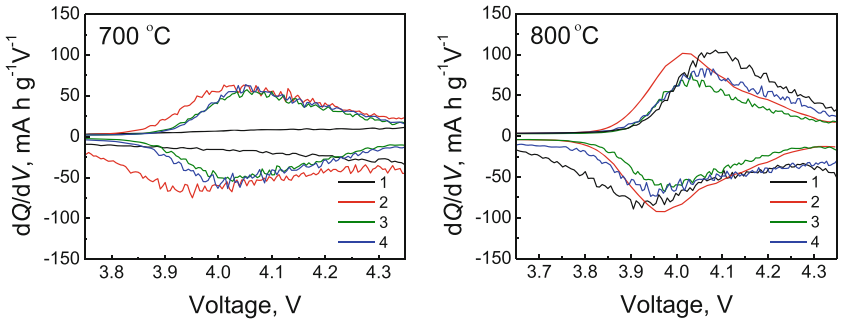

Fig. 10 dQ/dV vs. voltage plots in the 3.8–4.3 V range for $LiMn_{1.5}Ni_{0.5}O_4$ (*1*) and the Co- (*2*), Cr- (*3*), and Ti- (*4*) doped spinels prepared at 700 and 800 °C

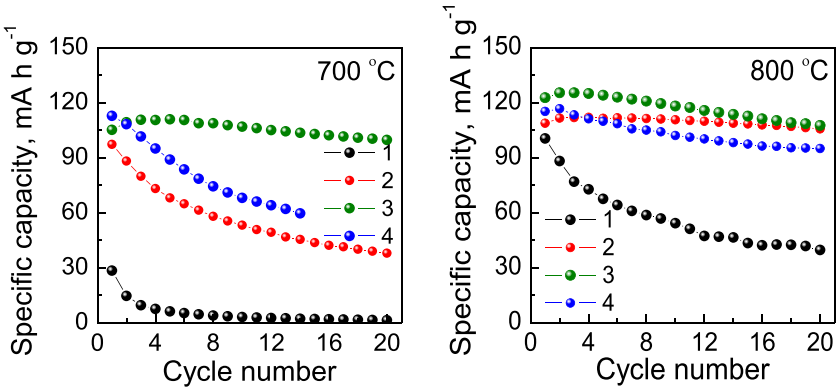

Fig. 11 Specific discharge capacity of $LiMn_{1.5}Ni_{0.5}O_4$ (*1*) and the Co- (*2*), Cr- (*3*), and Ti- (*4*) doped spinels prepared at 700 and 800 °C vs. the cycle number in the 3.0–4.85-V range

phase, and (4) the disproportionation reaction of the surface Mn^{3+} ions. Indeed, according to the structural study, these samples exhibit higher cationic Ni/Mn ordering and higher impurity content. The worst behavior revealed by the pure spinel is associated with nanosizing, resulting in the noticeable side reactions with the electrolyte. The protective surface modification is required in this case.

GITT

It is known that the Li ions in the disordered $LiNi_{0.5}Mn_{1.5}O_4$ spinel occupy the tetrahedral 8*a* sites and migrate via the vacant octahedral 16*c* sites in the 8*a*-16*c* diffusion paths. In the ordered spinel, the Li ions are located at the 8*c* sites and transfer via the 8*c*-4*a* and 8*c*-12*d* diffusion paths. This should affect the lithium diffusion coefficient. Amatucci et al. [4] showed that the disordered phase had the Li diffusion coefficient two orders of magnitude higher than the ordered counterpart.

GITT is extensively used to calculate the chemical diffusion coefficient. The classical application of this technique is related to the systems with the topotactic solid state intercalation reactions that lead to the formation of the solid-solution phases. It has been mentioned above that the disordered spinels exhibited the one-phase process from $x=1$ to $x\sim0.25$. This allows us to use the GITT measurements to obtain the equilibrium redox potentials and to evaluate the lithium

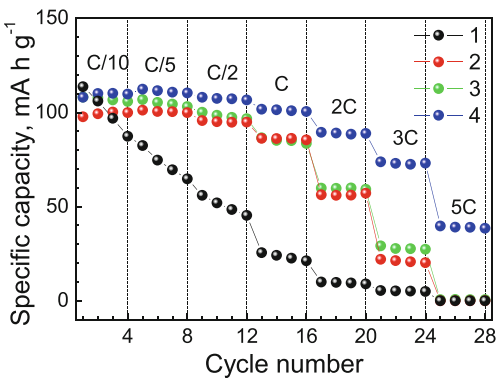

Fig. 12 Rate capability of $LiMn_{1.5}Ni_{0.5}O_4$ (*1*) and the Co- (*2*), Cr- (*3*), and Ti- (*4*) doped spinels prepared at 800 in the 3.0–4.85 V range

diffusion coefficient upon Li intercalation-deintercalation in the HT spinels.

Figure 13 shows the GITT curves of the undoped $LiNi_{0.5}Mn_{1.5}O_4$ and doped $LiNi_{0.5-x}Mn_{1.5-y}M_{x+y}O_4$ (M=Co, Cr, Ti) HT spinels obtained during the first cycle in the 3.0–4.85 V range, which illustrate the voltage dependence on the Li content under load and rest. The cell was charged and discharged at a constant current C/10 (I_0=14.7 mA g^{-1}) for an interval of 10 min followed by an open-circuit stand for 1 h to allow the cell voltage relaxing to its steady-state value (E_s). As seen, the Ni^{2+}/Ni^{3+} and Ni^{3+}/Ni^{4+} redox pairs in the spinels exhibit rather flat OCV profile. The short relaxation spikes observed for the doped spinels reveal fast reaction kinetics with a small polarization and fast equilibration as compared to the pure spinel. Note that the spikes are shorter for the charging curve demonstrating that the oxidation process is outperforming. It is supported by the asymmetry of the oxidation and reduction d*Q*/d*V* peaks in Fig. 9b: the oxidation peak areas are relatively larger than those of the reduction ones.

The lithium diffusion coefficient was calculated using Eq. (1), developed by Weppner and Huggins [33]:

$$D_{\mathrm{Li}}+ = \frac{4}{\pi}\left(\frac{V_M}{SF}\right)^2\left(I_0\frac{\delta E_s/\delta x}{\delta E/\delta t^{\frac{1}{2}}}\right)^2, \quad \text{at } t << \tau \qquad (1)$$

where V_M is a spinel molar volume (41 cm^3 mol^{-1}), *S* is a electrode surface area (13,500 cm^2 g^{-1}), *F* is the Faraday's constant (96,485 °C mol^{-1}), I_0 is a current pulse (0.047 A g^{-1}), $\delta Es/\delta x$ is a slope of the equilibrium open-circuit voltage vs. the Li content *x*, which can be obtained from the differential of the OCP curve, and $\delta E/\delta t^{1/2}$ is a slope of a voltage change vs. a square root of time.

The results of the GITT study are shown in Fig. 13. The calculated values of D_{Li+} during the charge-discharge processes are within the range from 10^{-16} to 10^{-14} cm^2 s^{-1} for the undoped spinel and from 10^{-14} to 10^{-12} cm^2 s^{-1} for all doped spinels, which is close to the results of Ref. [15]. Wan et al. [34] have calculated the diffusion coefficient using the CV data; it ranges from 7.72×10^{-11} to 2.01×10^{-10} cm^2 s^{-1}. One can notice an increase in the D_{Li} values by an order of

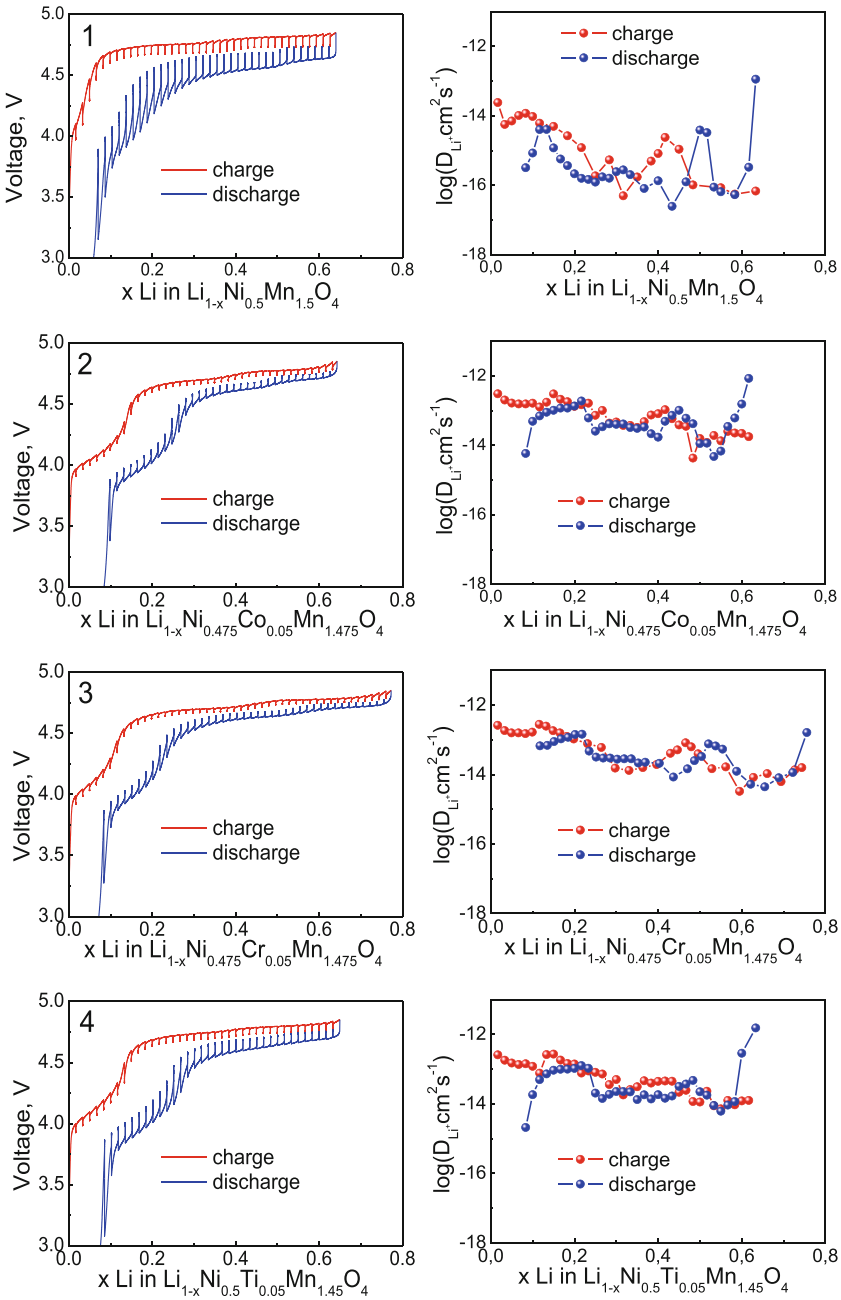

Fig. 13 GITT curves of $Li_xMn_{1.5}Ni_{0.5}O_4$ (*1*) and the Co- (*2*), Cr- (*3*), and Ti- (*4*) doped spinels prepared at 800 °C in the 3.0–4.85 V range and the calculated Li^+ diffusion coefficient D_{Li+} as a function of composition (*x*) during charge and discharge

magnitude at $x \sim 0.5$, corresponding to the bend on the 4.7 V plateau at the charge-discharge, which is a characteristic of the transition between two cubic phases [15]. We have recently observed the same phenomenon for the two two-phase transitions (Fe^{2+}/Fe^{3+} and Co^{2+}/Co^{3+}) in the $LiCo_{1-y}Fe_yPO_4$ solid solutions [35].

Conclusion

Thus, one-step mechanochemically assisted solid state synthesis of the $LiNi_{0.5-x}Mn_{1.5-y}M_{x+y}O_4$ spinels with the different dopant ions at a low concentration allows one to prepare the submicron cathode materials with the cubo-octahedral particle morphology and high degree of structural disordering at low synthesis temperature of 700–800 °C and for a short time duration. Neutron diffraction experiments have shown that the dopants preferably substituted Ni ions. In HT samples, the ordered phase is practically absent; the amount of the rock salt-structure impurity is 2–6 %. For the LT samples, the amounts of the ordered $P4_332$ phase, the $Li_yNi_{1-y}O$ impurity and the Mn^{3+} ions per formula unit average 5–10, 5–7 wt% and 0.12–0.14, respectively. Besides, the rock salt-structured phase was observed on the surface of the particles of the LT

samples coherently conjugated with the spinel crystal bulk and resulting in deterioration of electrochemical performance. The best high-rate capability is observed for the Ti-doped spinel, in a greater degree, owing to the enlarged lattice parameter.

Acknowledgments The work was partially supported by the Russian Foundation for Basic Research (Research project #14-02-31506). HRTEM studies were performed using the equipment of CCU "Nanostructures." The part of the work was carried out with the support of the Ministry of Education and Science of the Russian Federation (project ID RFMEFI62114X0004) and RSCF (project No. 14-22-00143). The authors are thankful to E.T. Devyatkina for the assistance with the preparation of the samples.

References

1. Santhanam R, Rambabu B (2010) J Power Sources 195:5442–5451
2. Lin GQ, Wen L, Liu YM (2010) J Solid State Electrochem 14: 2191–2202
3. Wang L, Li H, Huang X, Baudrin E (2011) Solid State Ion 193:32–38
4. Kunduraci M, Al-Sharab JF, Amatucci GG (2006) Chem Mater 18: 3583–3592
5. Cabana J, Casas-Cabanas M, Omenya FO, Chernova NA, Zeng D, Whittingham MS, Grey CP (2012) Chem Mater 24:2952–2964
6. Shin DW, Bridges CA, Huq A, Paranthaman MP, Manthiram A (2012) Chem Mater 24:3720–3731
7. Kim JH, Myung ST, Yoon CS, Kang SG, Sun YK (2004) Chem Mater 16:906–914
8. Kim JH, Huq A, Chi M, Pieczonka NPW, Lee E, Bridges CA, Tessema MM, Manthiram A, Persson KA, Powell BR (2014) Chem Mater 26:4377–4386
9. Oh SW, Myung ST, Kang HB, Sun YK (2009) J Power Sources 189:752–756
10. Ito A, Li D, Lee Y, Kobayakawa K, Sato Y (2008) J Power Sources 185:1429–1433
11. Alcantara R, Jaraba M, Lavela P, Tirado JL (2004) J Electrochem Soc 151:A53–A58
12. Arunkumar TA, Manthiram A (2005) Electrochim Acta 50:5568–5572
13. Liu D, Lu Y, Goodenough JB (2010) J Electrochem Soc 157: A1269–A1273
14. Alcantara R, Jaraba M, Lavela P, Tirado JL (2003) Chem Mater 15: 2376–2382
15. Kim JH, Myung ST, Yoon CS, Oh IH, Sun YK (2004) J Electrochem Soc 151:A1911–1918
16. Lin M, Wang SH, Gong ZL, Huang XK, Yang Y (2013) J Electrochem Soc 160:A3036–A3040
17. Xue L, Li X, Liao Y, Xing L, Xu M, Li W (2015) J Solid State Electrochem 19:569–576
18. Yang J, Han X, Zhang X, Cheng F, Chen J (2013) Nano Research 6: 679–687
19. Avvakumov E, Senna M, Kosova N (2001) Soft mechanochemical synthesis: a basics for new chemical technologies. Kluwer Acad Publ, Boston
20. Kosova NV (2010) High-energy ball milling. In: Sopicka-Lizer M (ed) Mechanochemical processing of nanoparticles. Woodhead Publ Ltd, Boca
21. Kosova NV, Devyatkina ET (2012) Russ J Electrochem 48:351–361
22. Oh SH, Jeon SH, Cho WI, Kim CS, Cho BW (2008) J Alloys Compd 452:389–396
23. Chen Z, Zhu H, Ji S, Linkov V, Zhang J, Zhu W (2009) J Power Sources 189:507–510
24. Kozawa T, Kondo A, Nakamura E, Abe H, Naito M, Koga H, Nakanishi S, Iba H (2014) Mater Lett 132:218–220
25. Shannon RD (1976) Acta Cryst A 32:751–767
26. Balagurov AM (2005) Neutron News 16:8–12
27. Cai L, Liu Z, An K, Liang C (2013) J Mater Chem A 1:6908–6914
28. Song J, Shin DW, Lu Y, Amos CD, Manthiram A, Goodenough JB (2012) Chem Mater 24:3101–3109
29. Glushko VP (ed) (1972) Thermal constants of substances, 6th and 7th edns. Nauka, Moscow
30. Lee E, Persson KA (2013) Nanotechnology 24:424007
31. Ariyoshi K, Iwakoshi Y, Nakayama N, Ohzuku T (2004) J Electrochem Soc 151:A296–A303
32. Lee E, Persson KA (2012) Energy Environ Sci 5:6047–6051
33. Weppner W, Huggins RA (1977) J Electrochem Soc 124:1569–1578
34. Wan L, Deng Y, Yang C, Xu H, Qin X, Chen G (2015) RSC Adv 5: 25988–25997
35. Kosova NV, Podgornova OA, Devyatkina ET, Podugolnikov VR, Petrov SA (2014) J Mater Chem A 2:20697–20705